INSTITUTTET FOR BYGNINGSTEKNIK
DEPT. OF BUILDING TECHNOLOGY AND STRUCTURAL ENGINEERING
AALBORG UNIVERSITETSCENTER • AUC • AALBORG • DANMARK

Lars Davidson
Implementation of a Large Eddy Simulation Method Applied to Recirculating Flow in a Ventilated Room
March 1996 **ISSN 1395-7953 R9611**

Implementation of a Large Eddy Simulation Method Applied to Recirculating Flow in a Ventilated Room

Lars Davidson
Thermo and Fluid Dynamics
Chalmers University of Technology
S-412 96 Gothenburg, Sweden

April 9, 1996

Abstract

In the present work Large Eddy Simulations are presented. The flow in a ventilated enclosure is studied. We use an explicit, two-steps time-advancement scheme where the pressure is solved from a Poisson equation. Second order accurate discretization is used in space and time. The pressure equation is solved using a pre-conditioned conjugate gradient method. First, the standard Smagorinsky model was used. It was found that the results were very dependent on the Smagorinsky constant. Therefore this model was abandoned and attention was turned towards the Dynamic model. The standard Dynamic model was implemented. In order to achieve numerical stability it was necessary to average the constant in the dynamic model in the spanwise direction. Furthermore, local averaging in the streamwise and spanwise direction has to be done. [1]

[1] This work was carried out during the author's stay at Dep. of Building Technology and Structural Engineering, Aalborg University in Autumn 1995.

Contents

1. Introduction

The Navier-Stokes equations are traditionally studied in their time-averaged form, often referred to as the Reynolds equations. The resulting unknown stresses $\overline{u_i u_j}$ stemming from the time averaging needs to be modelled with a turbulence model. The most common turbulence model is the two-equation $k-\varepsilon$ model [1]. In industry today, the $k-\varepsilon$ model is routinely used and the model is included in most commercial CFD-packages. The advantage of the $k-\varepsilon$ model from a numerical point of view is that it is robust and reliable. From a physical point of view the physics is treated in a simplistic manner, but nevertheless the model works surprisingly well in many types of flows.

However, there are physical phenomena which eddy viscosity models like the $k-\varepsilon$ model cannot capture such as streamline curvature and the effect of irrotational strains. Reynolds Stress Models (RSM) [2] do take this effects into account [3,4]. RSMs have been proven to be able to predict a number of types of flows better than $k-\varepsilon$ models. For a review, see Refs. [5–7]. Also Reynolds Stress Models are incorporated in many commercial CFD-codes, and RSMs are being increasingly used in the industry.

There seems to be a number of flows where the time averaged Navier-Stokes equations cannot be used, because too much information is filtered out in the time averaging process. Examples are transitional flows, either free or wall bounded, and separated flows where it is not appropriate to use the concept "mean" and "fluctuating" velocities as they are both of the same magnitude [8]. Flows around and behind bluff bodies is another example where the "mean" flow is not steady. These types of flows can probably be successfully predicted by Large Eddy Simulations (LES).

2. Large Eddy Simulations

2.1. Equations

With a spatial, inhomogeneous filter (denoted by a bar) applied to the incompressible Navier-Stokes equations, we obtain the momentum and continuity equations for the large scale motion

$$\frac{\partial \bar{u}_i}{\partial t} + \frac{\partial}{\partial x_j}\left(\bar{u}_i \bar{u}_j\right) = -\frac{1}{\rho}\frac{\partial \bar{p}}{\partial x_i} + \nu \frac{\partial^2 \bar{u}_i}{\partial x_j \partial x_j} - \frac{\partial \tau_{ij}}{\partial x_j} \tag{1}$$

$$\frac{\partial \bar{u}_i}{\partial x_i} = 0 \tag{2}$$

where the subgrid stresses are given by

$$\tau_{ij} = \overline{u_i u_j} - \bar{u}_i \bar{u}_j \tag{3}$$

2.2. Subgrid Models

We need a subgrid model to model the turbulent scales which cannot be resolved by the grid. In the present study we have chosen to use two types of models:

1. The simple model of Smagorinsky [9]
2. A dynamic subgrid model of Germano [10]

2.2.1. The Smagorinsky Model

The Smagorinsky model can be written [9]

$$\tau_{ij} - \frac{1}{3}\delta_{ij}\tau_{kk} = -2\nu_T \bar{S}_{ij} \tag{4}$$

$$\nu_T = (C_S \Delta)^2 \sqrt{2\bar{S}_{ij}\bar{S}_{ij}} \tag{5}$$

where $-\frac{1}{3}\delta_{ij}\tau_{kk}$ is included on the left-hand side to make the equation to be valid upon contraction (setting the induces i and j equal). The strain tensor $\bar{S}_{ij}$ is defined as

$$\bar{S}_{ij} = \frac{1}{2}\left(\frac{\partial \bar{u}_i}{\partial x_j} + \frac{\partial \bar{u}_j}{\partial x_i}\right) \tag{6}$$

and the filter-width is taken as the local grid size, i.e.

$$\Delta = (\Delta_{x,i}\Delta_{y,j}\Delta_{z,k})^{1/3} \equiv (\Delta V_{ijk})^{1/3} \tag{7}$$

where indices i, j, k denote cell-index in the three coordinate directions, and ΔV_{ijk} is the volume of the computational cell i, j, k.

Often a damping function is applied to the turbulent viscosity to account for viscous effects near walls. A standard form is chosen in this study which reads [11]

$$f_\mu = 1 - \exp\left(-\frac{n^+}{25}\right) \tag{8}$$

where $n^+ = u_* n/\nu$ (u_* and n denote friction velocity and normal wall distance, respectively).

The disadvantage of this model is that the constant C_S is unknown, and that it influences the calculated results very much. In the literature, the constant is found to vary in the range from $C_S = 0.065$ [12] to $C_S = 0.25$ [13].

2.2.2. The Dynamic Subgrid Model

Germano *et al.* [10,14] propose a *dynamic* subgrid model in which the constant C is not arbitrarily chosen (or optimized), but where it is *computed*. For convenience, the derivation of the Dynamic Subgrid Model given in Ref. [10] is repeated below. A second, coarser filter (test filter, denoted by $\widehat{\ }$) is applied to the equations. This size of the test filter (denoted by $\widehat{\Delta}$) is twice as coarse as the grid filter (Δ). When applying this second filter to Eq.1, we obtain

$$\frac{\partial \widehat{\bar{u}}_i}{\partial t} + \frac{\partial}{\partial x_j}\left(\widehat{\bar{u}}_i \widehat{\bar{u}}_j\right) = -\frac{1}{\rho}\frac{\partial \widehat{\bar{p}}}{\partial x_i} + \nu\frac{\partial^2 \widehat{\bar{u}}_i}{\partial x_j \partial x_j} - \frac{\partial T_{ij}}{\partial x_j} \tag{9}$$

where the subgrid stresses now are given by

$$T_{ij} = \widehat{\overline{u_i u_j}} - \widehat{\bar{u}}_i \widehat{\bar{u}}_j \tag{10}$$

Consider the resolved turbulent stresses $\mathcal{L}_{ij}$ defined as

$$\mathcal{L}_{ij} = \widehat{\bar{u}_i \bar{u}_j} - \widehat{\bar{u}}_i \widehat{\bar{u}}_j \tag{11}$$

which is representative of the contribution to the Reynolds stresses by the scales ℓ in the range between Δ and $\widehat{\Delta}$, i.e. $\Delta < \ell < \widehat{\Delta}$. From Eqs. 3,10,11 we obtain

$$\mathcal{L}_{ij} = T_{ij} - \widehat{\tau}_{ij} \tag{12}$$

Assume now that the functional form we use for the subgrid stresses for the τ_{ij} in the Smagorinsky model in Eq. 4 (grid filter level), also can be used to relate the subgrid stresses T_{ij} to $\widehat{\Delta}$ and $\widehat{\bar{S}}_{ij}$ at the test filter level. Combining Eqs. 4,5, we can write (note that while the Smagorinsky constant C_S in Eq.5 is squared, C is not)

$$\tau_{ij} - \frac{1}{3}\delta_{ij}\tau_{kk} = -2C\Delta^2|\bar{S}|\bar{S}_{ij} \tag{13}$$

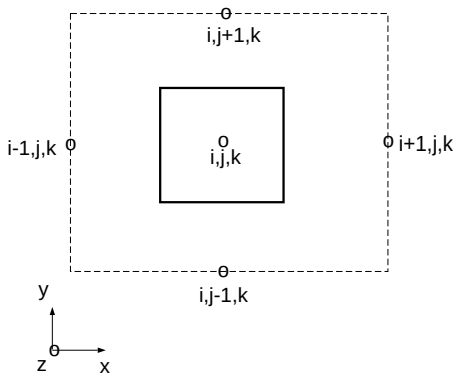

Figure 1. Grid cell (solid lines) and test cell (dashed lines).

$$T_{ij} - \frac{1}{3}\delta_{ij}T_{kk} = -2C\widehat{\Delta}^2 |\widehat{\bar{S}}|\widehat{\bar{S}}_{ij} \tag{14}$$

where

$$|\bar{S}| = \sqrt{2\bar{S}_{ij}\bar{S}_{ij}},\ \widehat{\bar{S}}_{ij} = \frac{1}{2}\left(\frac{\partial\widehat{\bar{u}}_i}{\partial x_j} + \frac{\partial\widehat{\bar{u}}_j}{\partial x_i}\right),\ |\widehat{\bar{S}}| = \sqrt{2\widehat{\bar{S}}_{ij}\widehat{\bar{S}}_{ij}} \tag{15}$$

Applying the test filter to Eq.13, substituting this equation and Eq.14 into Eq.11 gives

$$\mathcal{L}_{ij} - \frac{1}{3}\delta_{ij}\mathcal{L}_{kk} = -2C\left(\widehat{\Delta}^2|\widehat{\bar{S}}|\widehat{\bar{S}}_{ij} - \Delta^2\widehat{|\bar{S}|\bar{S}_{ij}}\right) \tag{16}$$

Note that the "constant" C really is a function of both space and time, i.e. $C = C(x_i, t)$. When deriving Eq.16 it has been assumed that the variation of C in space is slow, which allowed us to treat C as constant when applying the test filter to Eq.13.

Equation 16 is a tensor equation, which means that we have five (S_{ij} is symmetric and its trace is zero) equations for C. Germano *et al.* proposed to contract Eq. 16 with $\bar{S}_{ij}$ in order to reduce it to one equation. Later, Lilly [15] suggested to satisfy Eq. 16 in a least-square sense, defining the error Q

$$\begin{aligned} Q &= \left(\mathcal{L}_{ij} - \frac{1}{3}\delta_{ij}\mathcal{L}_{kk} - 2CM_{ij}\right)\left(\mathcal{L}_{ij} - \frac{1}{3}\delta_{ij}\mathcal{L}_{kk} - 2CM_{ij}\right) \\ M_{ij} &= -\left(\widehat{\Delta}^2|\widehat{\bar{S}}|\widehat{\bar{S}}_{ij} - \Delta^2\widehat{|\bar{S}|\bar{S}_{ij}}\right) \end{aligned}$$

requiring $\partial Q/\partial C = 0$, which gives

$$C = \frac{\mathcal{L}_{ij}M_{ij}}{2M_{ij}M_{ij}} \tag{17}$$

Following Germano *et al.* the ratio between the size of the test filter and the grid filter is set to two, i.e. $\widehat{\Delta}/\Delta = 2$ (see Fig. 1). The filtering procedure at the test level is carried out by integrating over the test cell assuming linear variation of the variables [16]. For $\widehat{\bar{u}}$, for example, we obtain

$$\widehat{\bar{u}}_{i,j,k} = \frac{1}{8}(\bar{u}_{i-1/2,j-1/2,k-1/2} + \bar{u}_{i+1/2,j-1/2,k-1/2}$$

$$\begin{aligned}
&\bar{u}_{i-1/2,j+1/2,k-1/2} \quad + \quad \bar{u}_{i+1/2,j+1/2,k-1/2} \\
&\bar{u}_{i-1/2,j-1/2,k+1/2} \quad + \quad \bar{u}_{i+1/2,j-1/2,k+1/2} \\
&\bar{u}_{i-1/2,j+1/2,k+1/2} \quad + \quad \bar{u}_{i+1/2,j+1/2,k+1/2})
\end{aligned}$$

2.3. Numerical Procedure

Equations 1 are solved with a finite volume procedure. Initially we tried to use an implicit SIMPLE code [17], but it turned out to be too expensive. In SIMPLE methods, one must iterate between the momentum equations and the pressure correction equation, and this required some twenty iterations on each time step, even though the Courant number

$$Co = \min\left\{\frac{U\Delta t}{\Delta_x}, \frac{V\Delta t}{\Delta_y}, \frac{W\Delta t}{\Delta_z}\right\} \tag{18}$$

was kept well below one. After that we started to work on an explicit method, which is described in this sub-section.

We want to solve Eqs.1. The convection and diffusion terms are discretized using a finite volume method [17,18] on a collocated grid. Second-order central differencing is used for both convection, diffusion and stresses. Having discretized these terms (denoted by H), the momentum equation (Eq.1) reads

$$\bar{u}_i^{n+1} = \bar{u}_i^n + \frac{\Delta t}{2\delta V}\left(3H^n - H^{n-1}\right) - \frac{\partial \bar{p}^{n+1}}{\partial x_i}\Delta t \tag{19}$$

where a second-order explicit time integration (often referred to as Adam-Bashfourth scheme) has been used for H, and where the time derivate has been discretized as

$$\int_{\Delta V} \frac{\partial \bar{u}_i}{\partial t} dV = \frac{\bar{u}^{n+1} - \bar{u}^n}{\Delta t}\Delta V \tag{20}$$

The problem is now that the pressure appears implicitly (level $n+1$) in Eq.19. To circumvent that problem, we follow the approach of Kim & Moin [19], and use a two-step time-advancement scheme. In step I the momentum equations are solved excluding the pressure gradient. Equation 19 is thus rewritten as

$$\bar{u}^* = \bar{u}_i^n + \frac{\Delta t}{2\delta V}\left(3H^n - H^{n-1}\right) \tag{21}$$

$$\bar{u}_i^{n+1} = \bar{u}_i^* - \frac{\partial \bar{p}^{n+1}}{\partial x_i}\Delta t \tag{22}$$

This gives us an intermediate velocity field $\bar{u}_i^*$ which does not satisfy the continuity equation. In order to satisfy continuity for $\bar{u}_i^{n+1}$, we take the divergence of Eq.22

$$\frac{1}{\Delta t}\frac{\partial}{\partial x_i}\left(\bar{u}_i^{n+1} - \bar{u}_i^*\right) = -\frac{\partial^2 \bar{p}^{n+1}}{\partial x_i \partial x_i} \tag{23}$$

But since we require $\bar{u}_i^{n+1}$ to satisfy the continuity equation, i.e.

$$\frac{\partial \bar{u}_i^{n+1}}{\partial x_i} = 0, \tag{24}$$

Eq.23 gives

$$\frac{\partial^2 \bar{p}^{n+1}}{\partial x_i \partial x_i} = \frac{1}{\Delta t} \frac{\partial \bar{u}_i^*}{\partial x_i} \tag{25}$$

Note that the pressure in Eq.19 is treated fully implicitly (level $n+1$) which is only first-order accurate in time, whereas in Ref. [19] they evaluated the pressure gradient using the Crank-Nicolson scheme (second-order accurate). We tried to use the Crank-Nicolson scheme for the pressure gradient, but we had numerical problems and did not obtain any stable solutions. The same experience is reported by Archambeau [20].

It should be noted that no numerical dissipation (such as Rhie-Chow interpolation [21]) is added to the equations.

Equation 25 is a Poisson equation for the pressure which must be solved each time step. In the present work it is solved with a conjugate gradient method with an incomplete Cholesky factorization as a preconditioner. The solver is a part of the `SLAP` package (Sparse Linear Algebra Package) available on `netlib`. This solver was implemented by Renard and Gresser [22]. It was found that it is very important to use a preconditioner, and that the incomplete Cholesky factorization was considerably more efficient than diagonal scaling. The incomplete Cholesky factorization is fairly expensive in terms of CPU, but fortunately the coefficients in the matrix stemming from the discretized Poisson equation (Eq.25) are constants, which means that we need to apply the preconditioner only the first time step.

The residual R expressed in L^2-norm

$$R = \frac{\sqrt{\sum_{ijk} \left(A_{ijk} p_{ijk} - b_{ijk}\right)^2}}{\sqrt{\sum_{ijk} \left(b_{ijk}\right)^2}}$$

is reduced to 10^{-3} at every time step, which requires approximately 90 % of the total CPU-time each time step.

The solution procedure can be summarized as follows:

$*1$. Solve the $\bar{u}, \bar{v}$ and $\bar{w}$ from Eq. 21 to obtain the intermediate velocity fields $\bar{u}^*, \bar{v}^*$ and $\bar{w}^*$.

$*2$. Compute the face velocities $\bar{u}^*_{i+1/2}, \bar{v}^*_{j+1/2}$ and $\bar{w}^*_{k+1/2}$ using linear interpolation.

$*3$. Compute the mass flux imbalance

$$\begin{aligned} \delta \dot{m} = (\bar{u}^*_{i+1/2} &- \bar{u}^*_{i-1/2}) \Delta y \Delta z \\ (\bar{v}^*_{j+1/2} &- \bar{v}^*_{j-1/2}) \Delta x \Delta z \\ (\bar{w}^*_{k+1/2} &- \bar{w}^*_{k-1/2}) \Delta x \Delta y \end{aligned}$$

$*4$. Solve the Poisson equation from Eq. 25 to obtain the pressure

$*5$. Correct the node velocities and face velocities

$*6$. Update velocities and pressure

$*7$. Compute the turbulent viscosity

$*8$. Goto next time step and repeat Step 1 to 8.

2.4. Boundary Conditions

For the pressure we use Neumann conditions at all boundaries, i.e.

$$\frac{\partial \bar{p}}{\partial n} = 0 \tag{26}$$

where n is the coordinate direction normal to the boundary. No-slip conditions is used for the velocities $\bar{u}_i$.

When using grids which are coarse near the floor (the $72 \times 42 \times 52$ mesh and the $102 \times 52 \times 52$, see Sub-section 5.2) we use wall functions at the walls. When the distance between the wall and the near-wall node exceeds 11 viscous units ($n^+ = 11$), the viscosity at the wall is set from the law of the wall [17], which corresponds to prescribing a wall shear stress τ_w according to the law of the wall. The Neumann condition in Eq. 26 requires no-slip conditions at the walls also for the intermediate velocity field $\bar{u}_i^*$ in order to satisfy global conservation in the Poisson equation (Eq.25) for the pressure [23,24].

3. $k - \varepsilon$ Model

In the present work we are also using the $k - \varepsilon$ model (steady calculations) for studying the influence of different grids, three-dimensional effects and for comparison. The standard $k - \varepsilon$ model is used which has the form

$$\begin{aligned}
U_j \frac{\partial k}{\partial x_j} &= \frac{\partial}{\partial x_j}\left(\frac{\nu_t}{\sigma_k}\frac{\partial k}{\partial x_j}\right) + P_k - \varepsilon \\
U_j \frac{\partial \varepsilon}{\partial x_j} &= \frac{\partial}{\partial x_j}\left(\frac{\nu_t}{\sigma_\varepsilon}\frac{\partial \varepsilon}{\partial x_j}\right) + \frac{\varepsilon}{k}\left(c_1 P_k - c_2 \varepsilon\right) \\
P_k &= \nu_t \left(\frac{\partial U_i}{\partial x_j} + \frac{\partial U_j}{\partial x_i}\right)\frac{\partial U_i}{\partial x_j} \\
\nu_t &= \nu + c_\mu \frac{k^2}{\varepsilon}
\end{aligned}$$

At the walls we use either standard wall functions [25] or a one-equation model. In the one-equation model by Wolfshtein [26], modified by Chen and Patel [27], the standard k equation is solved; the diffusion term in the k equation is modelled using the eddy viscosity assumption. The turbulent length scales are prescribed as:

$$\ell_\mu = c_\ell n \left[1 - exp\left(-R_n/A_\mu\right)\right] \tag{27}$$

$$\ell_\varepsilon = c_\ell n \left[1 - exp\left(-R_n/A_\varepsilon\right)\right]$$

(n is the normal distance from the wall) so that the dissipation term in the k equation and the turbulent viscosity are obtained as:

$$\varepsilon = \frac{k^{3/2}}{\ell_\varepsilon}, \quad \nu_t = c_\mu \sqrt{k} \ell_\mu$$

The Reynolds number R_n and the constants are defined as

$$R_n = \frac{\sqrt{k} n}{\nu}, \; c_\mu = 0.09, \;\; c_\ell = \kappa c_\mu^{-3/4}, \;\; A_\mu = 70, \;\; A_\varepsilon = 2 c_\ell$$

The one-equation model is used near the walls (the matching line is chosen along a pre-selected grid line where $y^+ \simeq 50$), and the standard high-Re $k - \varepsilon$ is used in the remaining part of the flow.

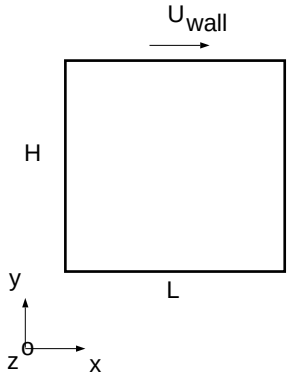

Figure 2. Two-dimensional lid driven cavity, $H = L$.

3.1. Numerical Method

The finite volume computer program CALC-BFC (**B**oundary **F**itted **C**oordinates) for three-dimensional complex geometries [17] is used. The solution procedure is based on SIMPLEC, and a collocated grid arrangement is employed. The convective terms in the mean flow equations are discretized using QUICK, a third-order scheme by Leonard [28]. For the turbulent quantities k and ε the hybrid central/upwind differencing scheme is used.

4. Results: Two-Dimensional Lid Driven Cavity

In this sub-section we validate our finite volume method presented in Sub-section 2.3 applied to two-dimensional flow in a lid driven cavity, see Fig. 2. Both steady and and unsteady calculations are carried out. The upper wall is moving with a constant velocity U_{wall}.

4.1. Steady Calculations

The Reynolds number is $Re = U_{wall}L/\nu = 3200$ and the predictions are compared with the benchmark calculation of Ghia *et al.* [29]. In Fig. 3 the U-profiles at $x/L = 0.5$ are presented, and as is seen the agreement is very good. To further validate the method we have carried out calculation on successively refined meshes with constant spacing. In Fig. 4 the U-velocity at $x/L = 0.5$, $y/H = 0.1016$ is compared with the corresponding velocity in Ref. [29]. For the convective terms we have used both central differencing and the QUICK scheme [28]. As can be seen the central differencing gives an accuracy of second order, as expected, and the QUICK scheme slightly better. It should be mentioned that whereas in Ref. [29] the point $y/H = 0.1016$ corresponds to (negative) velocity maximum, this is not the case in the present calculations. In Table 1 the maximum U-velocities and the velocities at $y/H = 0.1016$ are given.

4.2. Unsteady Calculations

Here we validate the code in unsteady flow for Reynolds number $Re = 400$. Central differencing is used for the convective terms. The predicted contours in Fig. 5 are compared with those predicted by Archambeau [20] where two different codes were used. The streamline contours presented in Fig. 5 are very similar to those in Ref. [20].

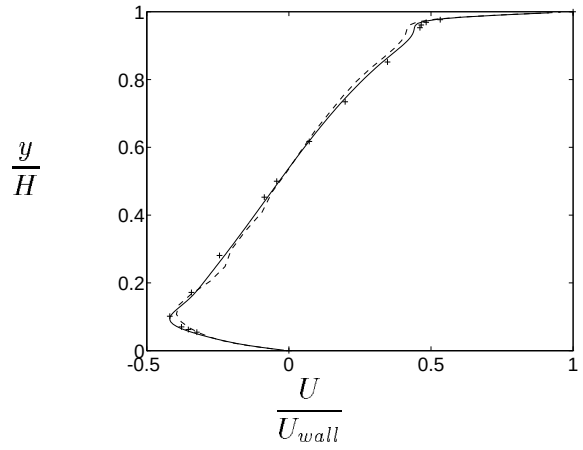

Figure 3. Predicted U-velocities at $x/L = 0.5$. Solid line: 160×160 mesh (central differencing) with constant spacing; dashed line: 40×40 mesh (QUICK) generated using hyperbolic tangent function (smallest cell size $\delta x/L = \delta y/H \simeq 0.003$); +: Benchmark results from Ghia *et al.* (1982).

	$U_{max}(y_{max})$	$U(y/H = 0.1016)$
20×20, **central**	-0.255(0.075)	-0.253
20×20, **QUICK**	-0.281(0.125)	-0.279
40×40, **central**	-0.322(0.1125)	-0.322
40×40, **QUICK**	-0.348(0.1125)	-0.341
80×80, **central**	-0.388(0.09375)	-0.387
80×80, **QUICK**	-0.402(0.10625)	-0.402
160×160, **central**	-0.419(0.096875)	-0.414
160×160, **QUICK**	-0.424(0.096875)	-0.418
Ghia *et al.* (1982)	-0.41933(0.1016)	-0.41933

Table 1
Max U-velocities and U-velocities at $y/H = 0.1016$.

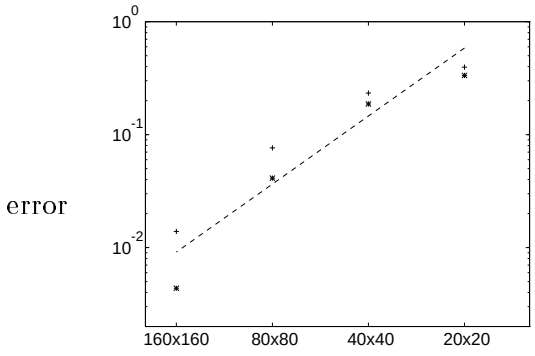

Figure 4. Predicted U-velocities at $x/L = 0.5$, $y/H = 0.1016$ using different meshes with constant mesh spacing. Error is defined as $(U - U_{bench})/U_{bench}$. +: central differencing; *: QUICK. Benchmark results from Ghia *et al.* (1982).

5. Results: Ventilated Room

In this section we predict the flow in a three-dimensional room, Fig. 6. The CALC-BFC code is used (see Section 3.1). The predictions are compared with Laser-Doppler measurements of Restivo [30] (also available in Ref. [31]). Inlet boundary conditions and the geometry are given by:

$$L/H = 3,\ W/H = 1,\ h/H = 0.056,\ t/H = 0.16,\ Re = \frac{U_{in} h}{\nu}$$

We have used $H = 3$, $U_{in} = 0.455$ m/s, and air of 20°C.

At the outlet the exit velocity is computed from global continuity and it is taken as constant over the outlet. Zero gradient is set for the remaining variables.

5.1. Predictions Using the $k - \varepsilon$ Model

The $k - \varepsilon$ model presented in Section 3 is used to compute the flow in the ventilated room. We are doing both two- and three-dimensional calculations. The inlet values of k and ε are given by [31]

$$k_{in} = 1.5\,(0.04 U_{in})^2\,;\ \varepsilon_{in} = k_{in}^{1.5}/\ell_{in},\ \ell_{in} = h/10$$

The QUICK scheme is used for the convective terms in the momentum equations, and the hybrid upwind/central scheme is used for k and ε. The predicted profiles in Fig. 8 turned out to be insensitive to the choice of discretization scheme for the momentum equations. Whether the second order van Leer scheme [32] was used for the k and ε equations or the hybrid upwind/central scheme was used in the momentum equations, the profiles in Fig. 8 remained virtually unchanged.

Computations have been carried out on a number of different grids. Here the results from two grids are presented, and they are shown in Fig. 7. For the two grids we use geometrically stretching in the y-direction, and a hyperbolic tangent function in the x-direction. For the 42×59 mesh Δy between the near-wall node and the ceiling is $\Delta y/H \simeq 6 \cdot 10^{-5}$ and at the floor $\Delta y/H \simeq 0.014$. Near the vertical walls we have $\Delta x/H \simeq 0.01$. The two-layer model is used near the ceiling, and at the other boundaries wall functions are used. For the 72×42 mesh Δy at the ceiling is $\Delta y/H \simeq 0.0026$ and at the floor $\Delta y/H \simeq 0.014$. The corresponding figure near the vertical walls is $\Delta x/H \simeq 0.018$, but the stretching in the x-direction is much smaller for this grid (see Fig. 7). Wall functions are

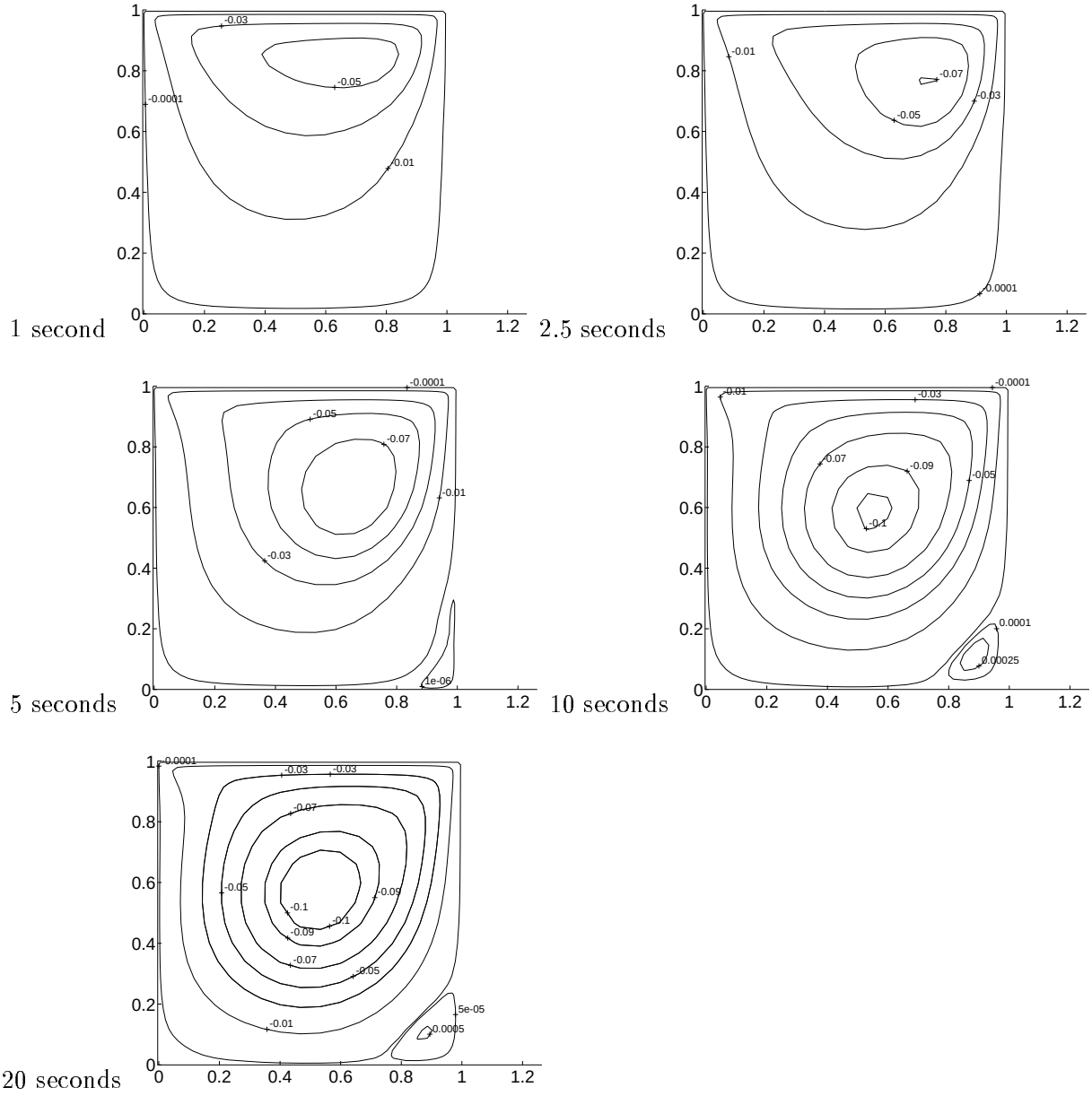

Figure 5. Streamline contours at different times.

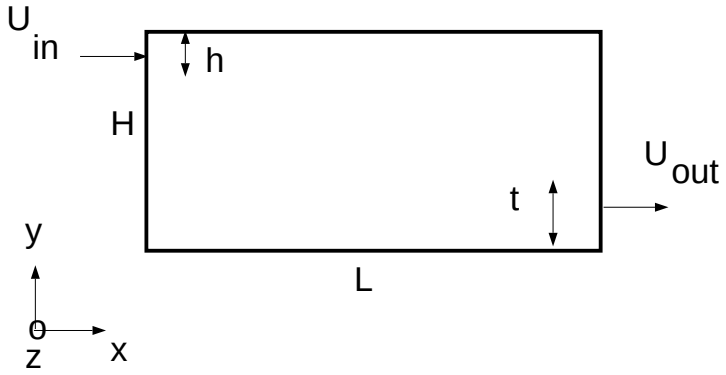

Figure 6. Ventilated room.

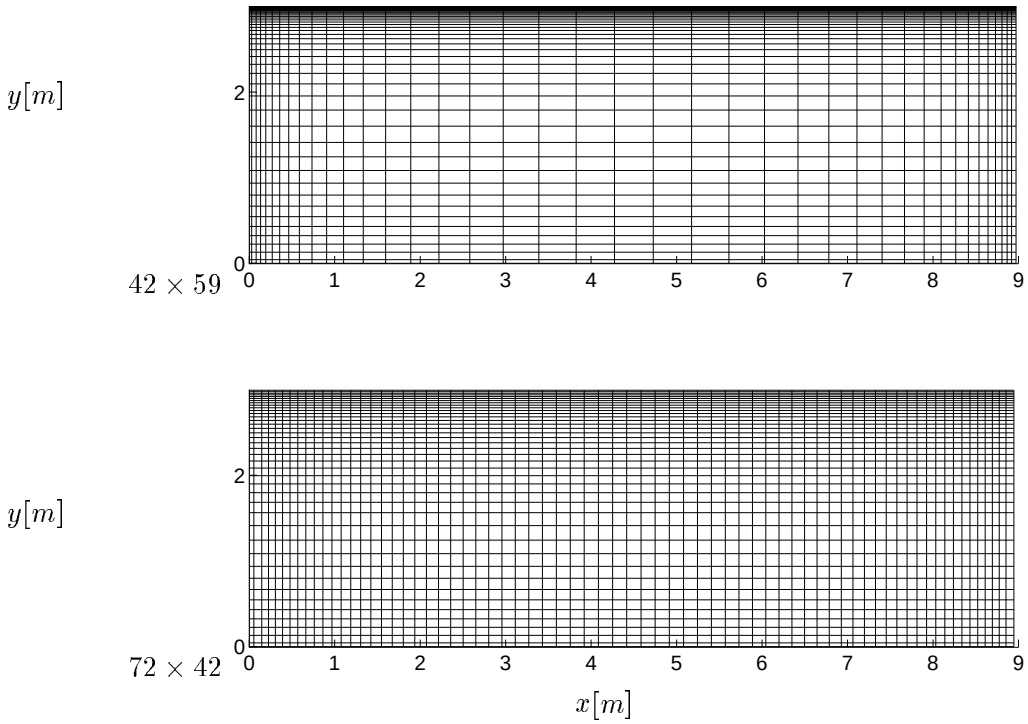

Figure 7. Grids for two-dimensional calculations using $k - \varepsilon$.

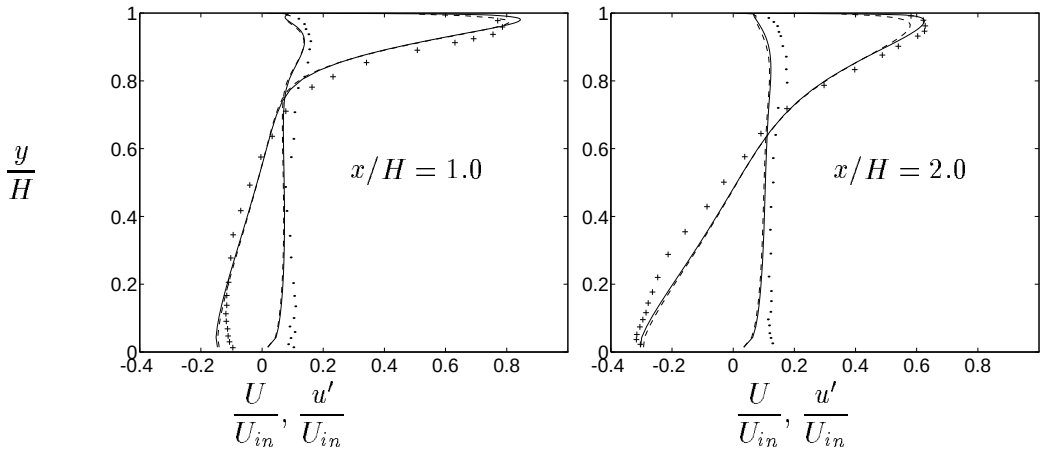

Figure 8. U-profiles and u'-profiles. Two-dimensional calculations. Solid lines: 42×59 mesh; dashed lines: 72×42 mesh; +: experimental U/U_{in}; ·: experimental u'/U_{in}.

used at all solid boundaries. The two grids that are used are rather coarse, but they are relevant for three-dimensional LES calculations.

The U velocities and the streamwise rms velocities are shown in Fig. 8 and the agreement between the prediction and experiments is fairly good. The predicted streamwise rms velocity is obtained as $u' = (2k/3)^{0.5}$. The predicted peak velocity in the wall jet differ by some 6 % using the two different grids. In the remaining part of the room the two grids give almost identical results.

To further prepare for the LES calculations we have also carried out some three-dimensional calculation using the $k - \varepsilon$ model. Three different extents of the domain in the z-direction have been used: $W/H = 0.5, 1.0$ and $W/H = 4.7$. Here we present calculations obtained using the 42×59 mesh in the $x - y$ plane and using 16, 30 and 60 cells, respectively for the three widths, with constant spacing in the z-direction, respectively for the three widths. In Fig. 9 the predicted profiles are compared with measurements. When plotting the profiles for $W/H = 4.7$ and the two-dimensional results obtained with the 42×59 mesh the profiles are, as expected, identical. The smaller the width, the larger effect the boundary layers on the side walls will have. That is also seen in Fig. 9 where the velocities both in the wall jet and in the back flow region decreases as W increases. In Fig. 10 the velocity profiles are shown in greater detail near the floor and the ceiling.

5.2. Large Eddy Simulations

The explicit code described in Sub-section 2.3 is used. A steady computation is first carried out using the CALC-BFC code and the $k - \varepsilon$ mode (as in Section 5). These results are used as initial start fields in the LES calculations. The number of time steps used in each calculation is typically 40000, which for the $72 \times 42 \times 26$ is approximately 900 seconds when using the dynamic model. The streamwise average of the peak velocity in the wall jet along the ceiling is close to $U_{av} = 0.5U_{in}$ ($= 0.228$ m/s). Thus the time it takes for fluid particle to move from the inlet to the opposite wall can be estimated as $L/U_{av} \simeq 40$ seconds, which means that $900/40 \simeq 22.5$ characteristic time units (L/U_{av}) are covered in a simulation.

Since we resolve the large-scale turbulence we should impose turbulent flow conditions at the inlet. As an approximation random fluctuations are superimposed on the time-averaged experimental flow

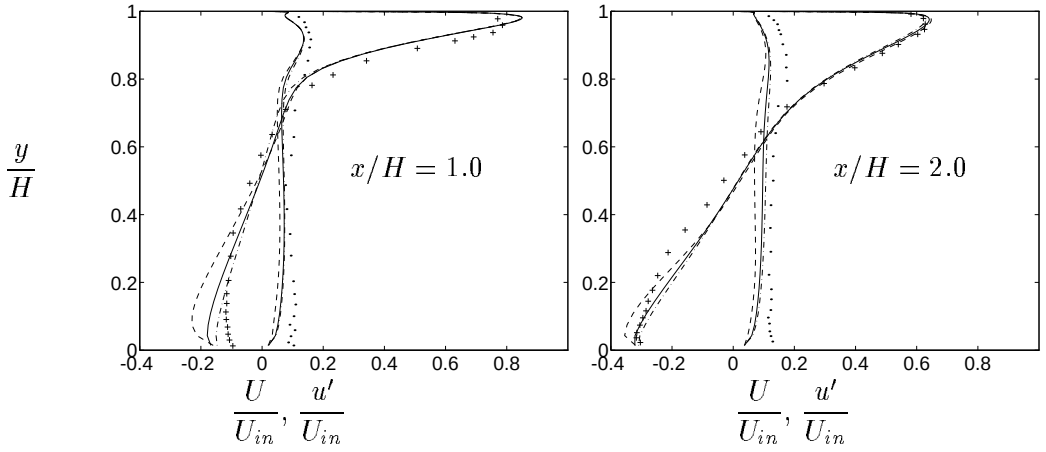

Figure 9. U-profiles and u'-profiles in the symmetry plane $z/H = 0.5$. Three-dimensional calculations. Dashed lines: $W/H = 0.5$; solid lines: width $W/H = 1.0$; dash-dotted lines: $W/H = 4.7$; $+$: experimental U/U_{in}; $\cdot$: experimental u'/U_{in}.

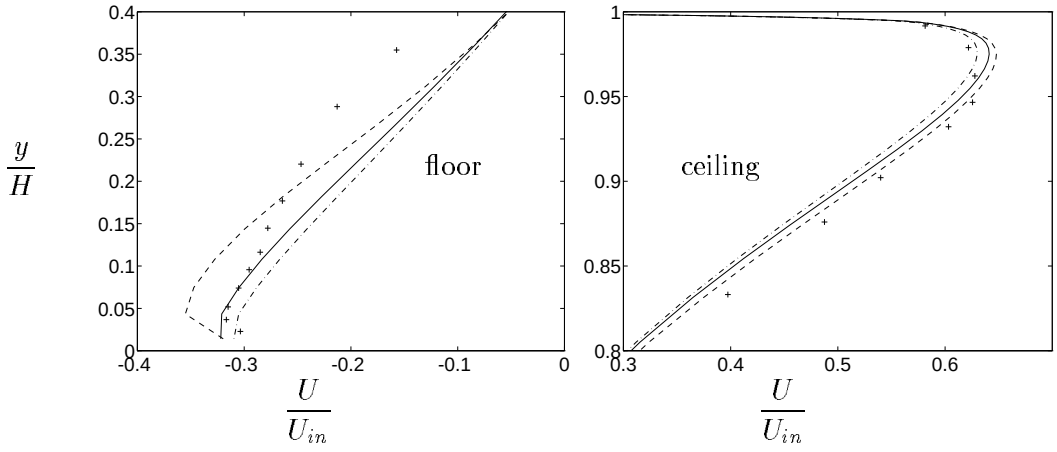

Figure 10. Zoomed view of U-profiles near the floor and the ceiling. Symmetry plane $z/H = 0.5$ at $x/H = 2.0$. Three-dimensional calculations. Dashed lines: $W/H = 0.5$; solid lines: width $W/H = 1.0$; dash-dotted lines: $W/H = 4.7$; $+$: experimental U/U_{in}.

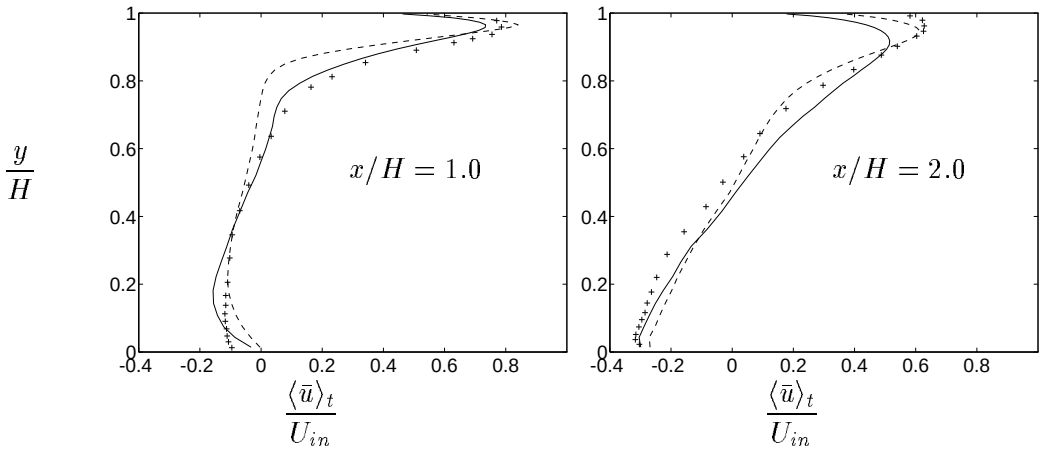

Figure 11. Time averaged velocity profiles. Symmetry plane $z/H = 0.5$. LES using the Smagorinsky model. Mesh: $72 \times 52 \times 26$. Solid lines: $C_S = 0.14$; dashed lines: $C_S = 0.18$; +: experimental U/U_{in}.

conditions at the inlet according to:

$$\bar{u}_{in} = U_{in} + random \cdot u'_{exp},\ \bar{v}_{in} = random \cdot u'_{exp},\ \bar{w}_{in} = random \cdot u'_{exp} \tag{28}$$

Note that the random function is called at different times for $\bar{u}_{in}$, $\bar{v}_{in}$ and $\bar{w}_{in}$, which means that the fluctuations are not correlated. This means, furthermore, that the shear stresses $\overline{\bar{u}\bar{v}}$, $\overline{\bar{u}\bar{w}}$ and $\overline{\bar{v}\bar{w}}$, are set to zero at the inlet.

The maximum CFL number is for stability reasons set to 0.4.

5.2.1. Using the Smagorinsky Model

In Fig. 11 the time averaged ($\langle \cdot \rangle_t$ denotes time averaging) predicted velocity profiles are compared with experiments. Prediction with two different values on the constant C_S are shown in Fig. 11, and as can be seen the solutions differ considerable. Thus it seems that when using this model the constant C_S must first optimized, and this value is probably both flow dependent as well as grid dependent. This is the reason why this model was abandon in the present work and attention was shifted to the dynamic model.

5.2.2. Using the Dynamic Model

Three different meshes have been used: $72 \times 52 \times 26$, $72 \times 42 \times 52$ and $102 \times 52 \times 52$. For all three meshes geometrical stretching is used in y-direction, and a hyperbolic tangent function is used in x and z-direction. They are summarized in Table 2.

It is well known that when using the dynamic model one must set some limits on C in Eq. 17 or do some averaging in order to achieve numerical stability. In the present study we average C in the spanwise (z) direction. This was found not to be enough. In addition we had to average C in x ($i = \pm 2$) and y-direction ($j = \pm 2$). Furthermore the total (laminar plus turbulent) viscosity is not allowed to become negative. No maximum limit on C (or viscosity) was used. This procedure is similar to that chosen in Ref. [33].

When comparing with experiments we must time average over a certain time T in the same way experimentalists measure over a certain time when they are recording a turbulent signal. The question is when we should start to time average (T_0) and for how long (T). In Fig. 12 we investigate the influence of T_0 and T on the time averaged $\bar{u}$-profile. In general the $\langle \bar{u} \rangle_t$ does not seem to be very

Mesh	$\Delta x_{min}/H$	$\Delta y_{min,f}/H$	$\Delta y_{min,c}/H$	$\Delta z_{min}/H$	$\Delta x_{max}/H$	$\Delta y_{max}/H$	$\Delta z_{max}/H$
72x52x26	0.005	0.008	0.002	0.006	0.09	0.038	0.082
72x42x52	0.018	0.014	0.0027	0.0024	0.06	0.042	0.042
102x52x52	0.005	0.008	0.002	0.0027	0.06	0.038	0.041

Table 2
Geometrical details of the three meshes used in combination with the dynamic model. The *min* distances are from the near-wall node to the boundary. Index c and f denote ceiling and floor, respectively. Along the centerline at the ceiling the friction velocity is approximately $u_*/U_{in} \simeq 0.04$

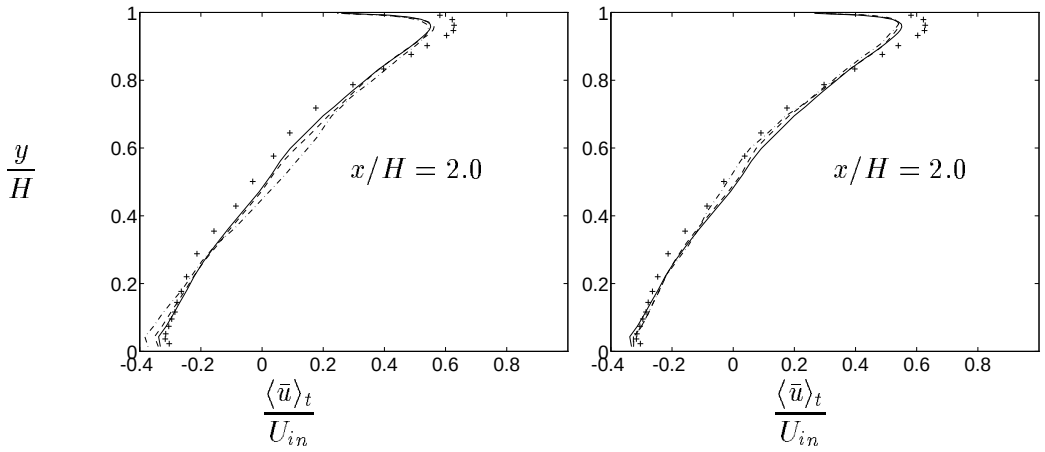

Figure 12. Influence of averaging time T on time averaged velocity profiles. 2000 time steps have been performed before starting averaging. $72 \times 42 \times 52$ mesh. Symmetry plane $z/H = 0.5$. LES using the dynamic model. +: experimental U/U_{in} velocity. a) $T_0 = 0$. Solid lines: $T = 881$ seconds (40000 time steps); dashed lines: $T = 427$ seconds (the first 20000 time steps); dash-dotted lines: $T = 204$ seconds (the first 10000 time steps). b) $T = 881$ (40000 time steps). Solid lines: $T_0 = 0$; dashed lines: $T_0 = 427$ seconds (the last 20000 time steps); dash-dotted lines: $T_0 = 204$ seconds (the last 10000 time steps).

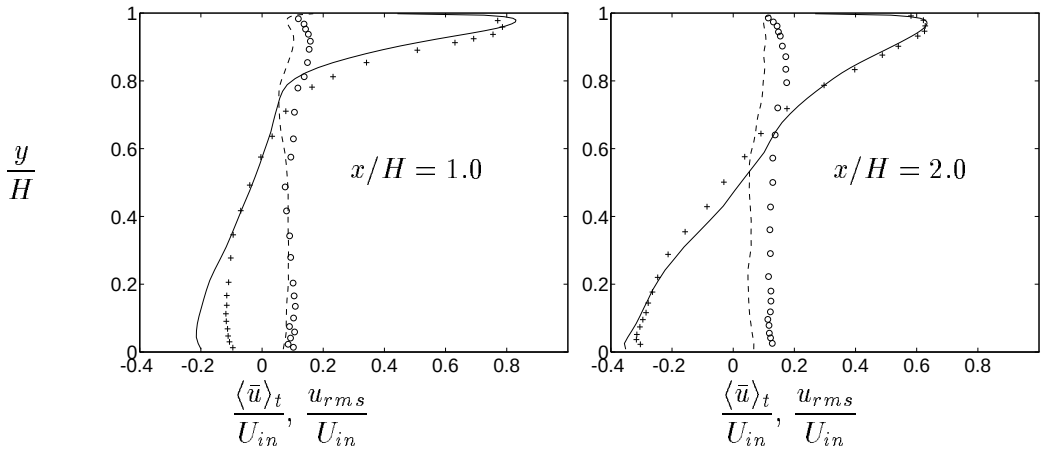

Figure 13. Time averaged velocity and resolved rms velocity profiles. $72 \times 52 \times 26$ mesh. Symmetry plane $z/H = 0.5$. LES using the dynamic model. Solid lines: $\langle \bar{u} \rangle_t / U_{in}$; dashed lines: u_{rms}/U_{in}; +: experimental mean velocity; *o*: experimental fluctuations.

sensitive to the choice of T and T_0, but the differences are largest close to $y/H = 0.5$. This has also been found in experimental investigations, where longer measuring times must be used in the middle of the room (low-speed regions) than near walls (high-speed regions)[2] When reducing the time averaging to the first 10000 time steps (Fig. 12a) the magnitude of $\langle \bar{u} \rangle_t$ starts to increase close to the floor.

In Figs. 13-15 the predicted velocity profiles using the three different meshes are compared with experiments. It can be seen that the agreement with experiments is fairly good for all meshes, but that the solutions are grid dependent. In general the resolved rms fluctuations

$$u''(t) = \bar{u}(t) - \langle \bar{u}(t) \rangle_t$$

$$u_{rms} = \sqrt{\langle (u''(t))^2 \rangle_t}$$

are under-predicted. The $\langle \bar{u} \rangle_t$ profiles along the ceiling (at $y = H - y/2$) and the floor (at $y = y/2$) are shown in Fig. 16. The agreement between predictions and experiments is fairly good. The recirculation bubble along the ceiling close to the opposite wall is over-predicted compared to experiments. Furthermore it can be seen that there is a large difference in the flow along the floor when using the two grids. The coarse grid severely under-predicts the $\langle \bar{u} \rangle_t$ velocity. The fine grid gives a much closer agreement with experiments. However, the fine grid predicts a separation along the floor at $x/H \simeq 1.2$ which is too early according to experimental data. Downstream ($0.3 < x/H < 1.2$) there is a stagnant region with $\langle \bar{u} \rangle_t$ velocities close to zero, which also can be seen in Fig. 18b.

The instantaneous velocity vectors in two planes are shown in Fig. 17. The zoomed view in Fig. 17a shows a wavy flow field below the ceiling which is generated by the resolved fluctuations, and which generates high shear stresses in the wall jet and entrains stagnant fluid into the wall jet. Higher turbulent viscosity, i.e. higher value on C in Eq. 17, damps the resolved fluctuations and the entrainment which means that the velocity profile close to the velocity maximum will be thinner with a higher, sharper peak. This is confirmed in Fig. 11 where a large value on C_S in the Smagorinsky model gives a thin velocity profile in the wall jet with a high peak value. Note that this is vice versa to what we

[2]Hyldgård, C.E., private communication, Dep. of Building Technology and Structural Engineering, Aalborg University

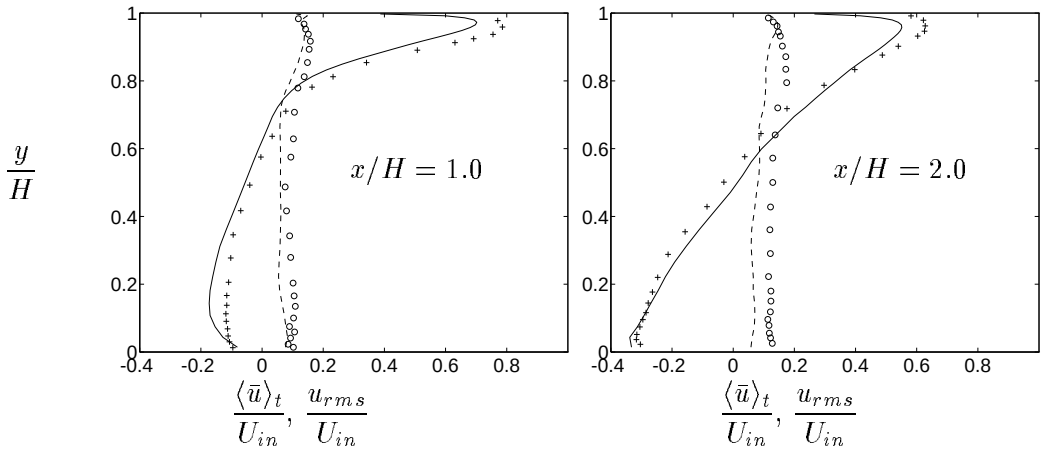

Figure 14. Time averaged velocity and resolved rms velocity profiles. $72 \times 42 \times 52$ mesh. Symmetry plane $z/H = 0.5$. LES using the dynamic model. Solid lines: $\langle \bar{u} \rangle_t / U_{in}$; dashed lines: u_{rms}/U_{in}; $+$: experimental mean velocity; o: experimental fluctuations.

are used to when using traditional eddy viscosity models where high turbulent viscosity is connected with flat, smeared-out velocity profiles.

Some longitudinal vortices are visible in Fig. 17b. It seems like the mesh is too coarse in the z-direction. Near the ceiling in the middle it looks like the flow is trying to form longitudinal vortices, but that the grid resolution is insufficient. From Table 2 we find that the maximum cell-size in the spanwise direction expressed in viscous units is $\Delta z_{max} u_* / \nu \simeq 150$. From experiments [34] and DNS-simulations [35] it is known that the width (diameter) of these longitudinal vortices, caused by alternating low- and high-speed streaks in the spanwise direction, is around 100 viscous units. Clearly the meshes used in the present work is too coarse to capture these phenomena. As noted by Piomelli [36], it may not be necessary to capture these effects if we only are interested in mean velocities and rms fluctuations.

In Fig. 18 zoomed views of vector plots in the upper-right and the lower-left corners are presented. The recirculation bubble near the ceiling is nicely captured. In the recirculation bubble near the floor the velocities are much smaller ($< 0.03 U_{in}$), and we can see three vortices.

The resolved $\bar{u}$ velocities versus time at four chosen points are presented in Fig. 19. It can be seen that the fluctuations in $\bar{u}$ are strong. In the middle of the room (Fig. 19b) it is not meaningful to define a "mean" velocity $\langle \bar{u} \rangle_t$, since $\bar{u}/U_{in}$ fluctuates between 0.15 and -0.23 and the time averaged velocity is close to zero. It can also be seen that the frequency of $\bar{u}$ is much higher in the wall jet near the ceiling (Figs. 19a,c) than in the back-flow region close to the floor (Fig. 19d). In addition to the large-scale fluctuations visible in Fig. 19 we have small-scale fluctuations which can be seen in Fig. 20. These small-scale fluctuations are generated by the inlet boundary conditions, where a randomized velocity field is prescribed (see Eq. 28). If constant flow conditions (in time) are prescribed, the small-scale fluctuations go away. Also the time history of the $\bar{u}$ velocities (like that shown in Fig. 19) becomes less chaotic.

In Fig. 21 the C coefficient in the dynamic model (see Eq. 17) is presented. Figure 21a shows the time history of C at two chosen points, one point in the wall jet close to the ceiling, and one point in the boundary layer close to the floor. The variation of C is fairly big, especially close to the floor where the amplitude of the fluctuations is larger than $\langle C \rangle_t$. It should be noted that at these two chosen

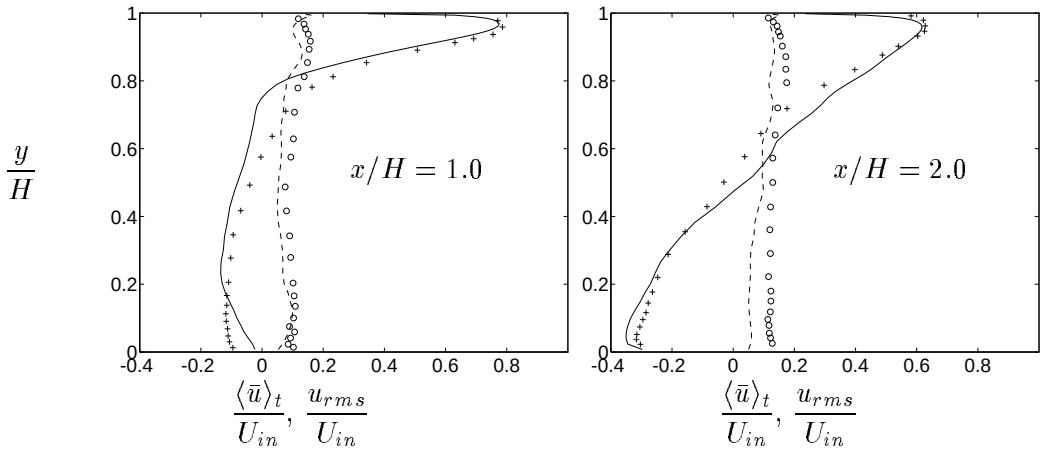

Figure 15. Time averaged velocity and rms velocity profiles. $102 \times 52 \times 52$ mesh. Symmetry plane $z/H = 0.5$. LES using the dynamic model. Solid lines: $\langle \bar{u} \rangle_t / U_{in}$; dashed lines: u_{rms}/U_{in}; +: experimental mean velocity; *o*: experimental fluctuations.

point it is only at $t \simeq 260$ that C goes negative. (As mentioned in the beginning of Sub-section 5.2.2 the total viscosity is not allowed to go negative.) In Fig. 21b the instantaneous C versus y is shown, and it can be seen that C is small at the floor and ceiling as it should. The average value of C in the y-direction is approximately 0.04 which in the Smagorinsky model corresponds to

$$C_S = \sqrt{C} = 0.2$$

The present values on C are smaller than those obtained by Zang *et al.* [16] and approximately two times larger than those found by Yang and Ferziger [33], which confirms that C is flow dependent.

The point of separation x_{sep} along the ceiling and the floor are shown in Fig. 22. The spanwise averaged values are shown (solid lines). The frequency of x_{sep} is similar to that of the velocity itself. The location of separation along the ceiling is fluctuating very much whereas it is more stable along the floor. In Fig. 16 the $\bar{u}$-velocities at the centerline along the ceiling ($y = H - h/2$) and the floor ($y = h/2$) are shown. The dotted lines in Fig. 22 show the x-location where those $\bar{u}$-velocities change sign versus time. It occurs both close to the ceiling and close to the floor that $\bar{u}$ does not change sign but that the flow continues all the way to the opposite wall. It happens only once close to the ceiling ($t \simeq 120$ in Fig. 22a) but several times close to the floor.

The two-point correlation coefficient $R_{u'',u''}(y, y_0)$ [37]

$$R_{u'',u''}(y, y_0) = \frac{\langle u''(y) u''(y_0) \rangle_t}{\sqrt{\langle (u''(y))^2 \rangle_t} \sqrt{\langle (u''(y_0))^2 \rangle_t}} \tag{29}$$

is shown in Fig. 23. Using the two-point correlation coefficient we can compute the integral length scale Λ from [37]

$$\Lambda = \int_{y_1}^{y_2} R_{u'',u''}(y, y_0) dy. \tag{30}$$

The integration limits are taken at the point y_0 and away from the wall, which means that for the points at $y/H = y_0/H = 0.92$ we have $y_1/H = 0.92$, $y_2 = 0$, and for the points at $y/H = y_0/H = 0.14$ we use $y_1/H = 0.14$, $y_2/H = 1.0$. The integral length scales for four points are given in Table 3.

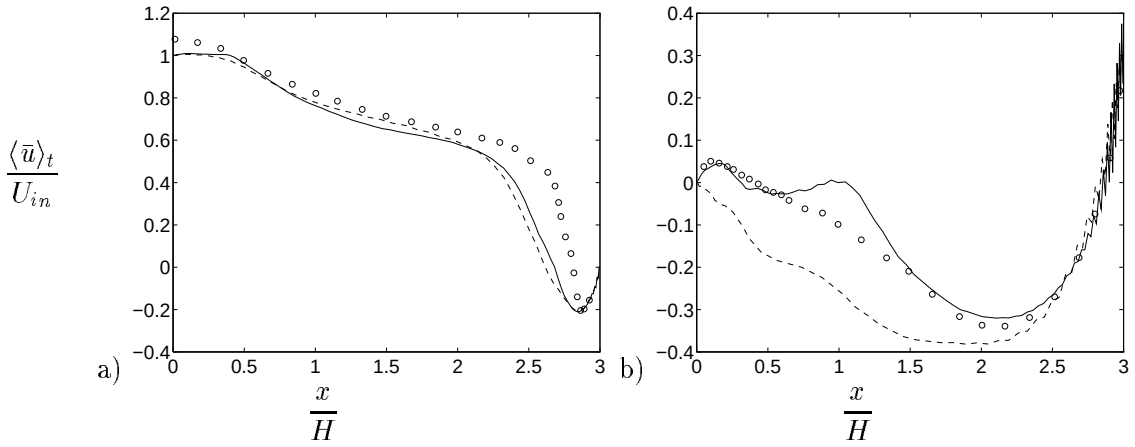

Figure 16. Time averaged $\bar{u}$ velocity along the ceiling and the floor. The dynamic model. $z/H = 0.5$. Solid line: $102 \times 52 \times 52$ mesh; dashed lines: $72 \times 52 \times 26$ mesh; o: experiments. a) $y = H - h/2$. b) $y = h/2$.

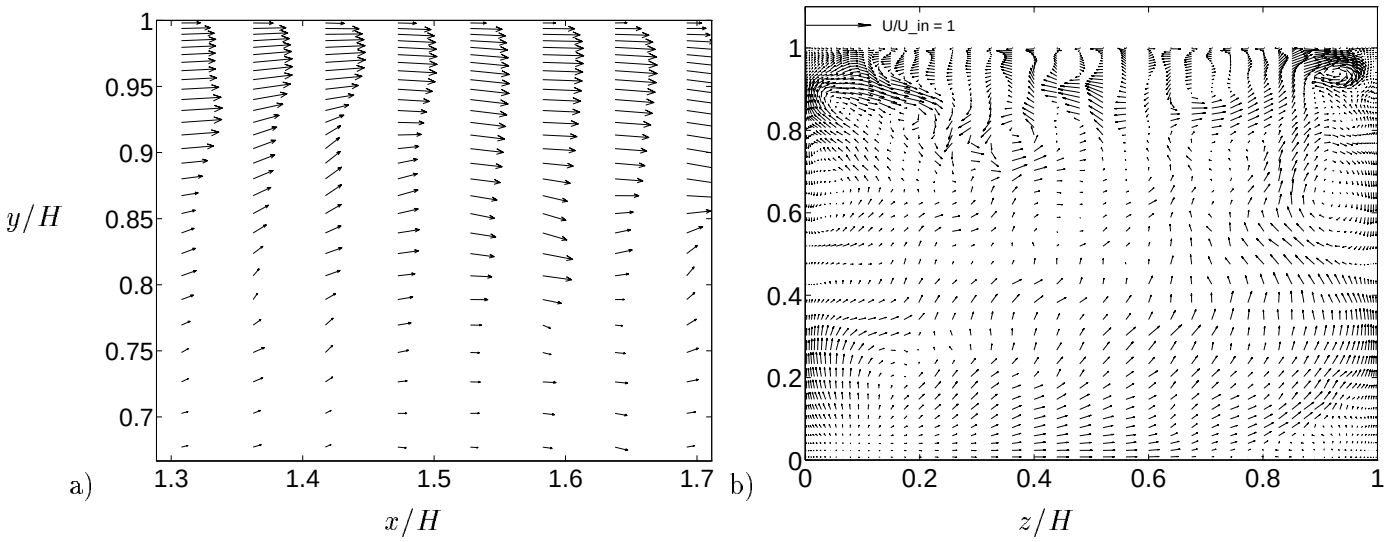

Figure 17. Velocity vectors at a given time. $102 \times 52 \times 52$ mesh. LES using the dynamic model. a) $z/H = 0.5$. b) $x/H = 1.5$.

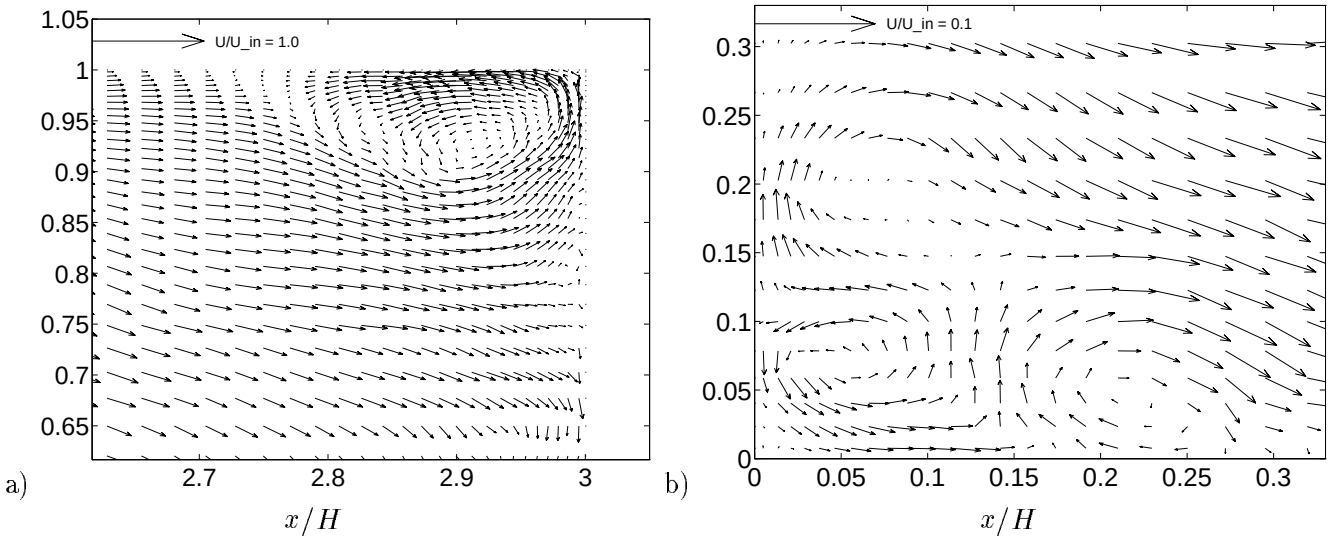

Figure 18. $102 \times 52 \times 52$ mesh. Instantaneous velocity vectors. $z/H = 0.5$. a) upper-right corner. b) lower-left corner.

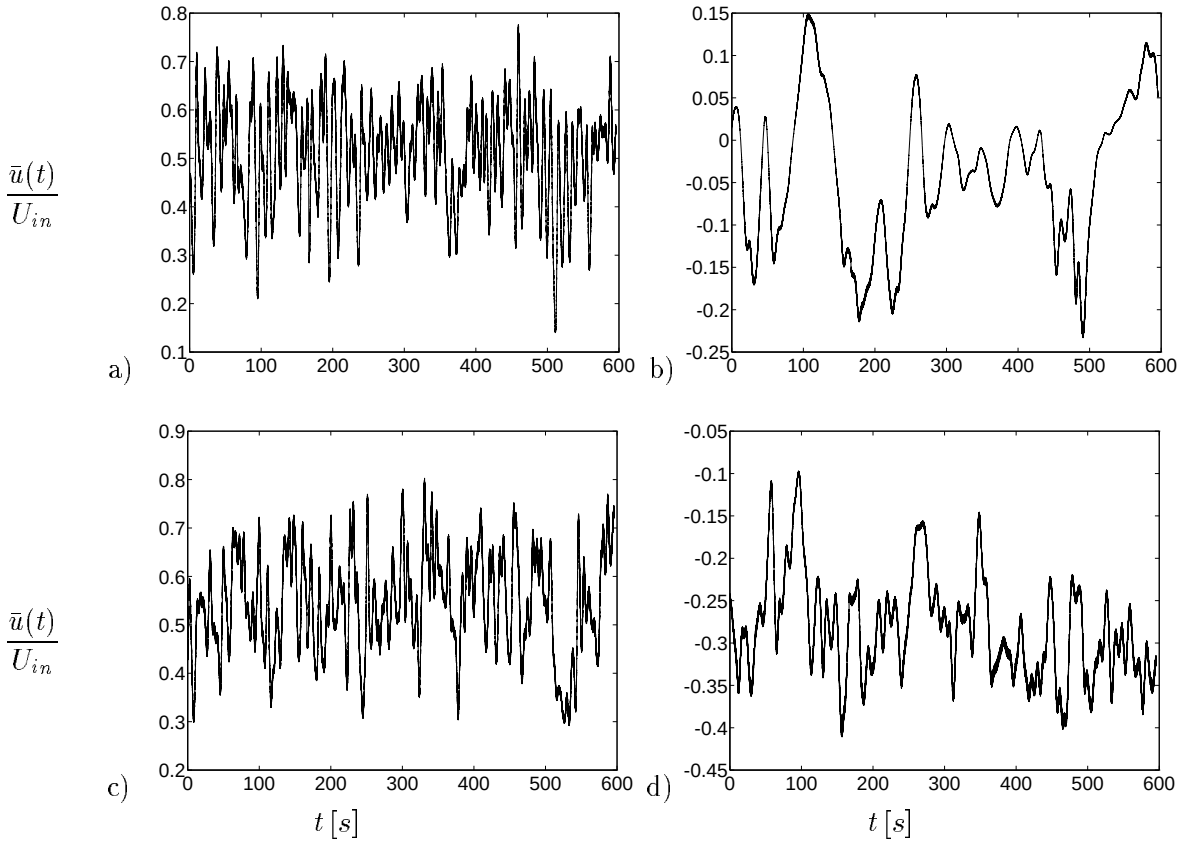

Figure 19. Time history of the $\bar{u}$ at four chosen cells. $72 \times 52 \times 26$ mesh. $z/H = 0.5$. Dynamic model. a) $x/H = 1.0, y/H = 0.92$, b) $x/H = 1.0, y/H = 0.5$, c) $x/H = 2.0, y/H = 0.92$, d) $x/H = 2.0, y/H = 0.14$.

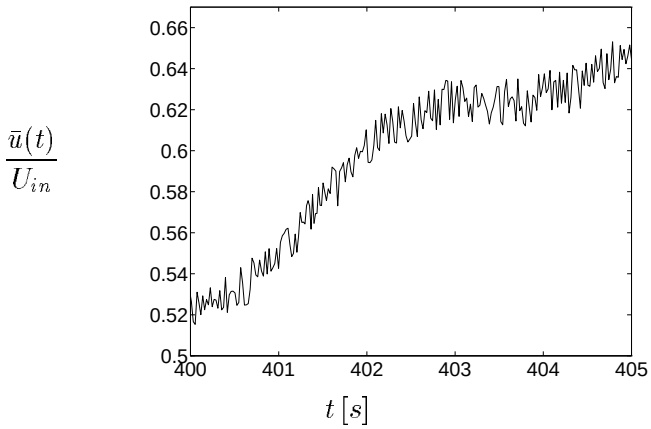

Figure 20. Time history of the $\bar{u}$ at $x/H = 2.0, y/H = 0.92, z/H = 0.5$ during a short time. $72\times52\times26$ mesh. Dynamic model.

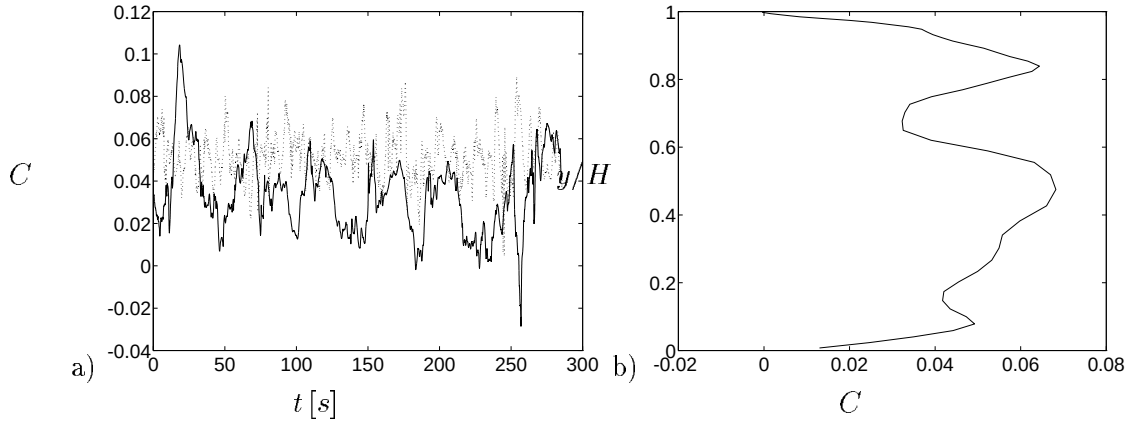

Figure 21. The C coefficient in the dynamic model. $x/H = 1.0, z/H = 0.5$. $102 \times 52 \times 52$ mesh. a) Time history of C at two points. Solid line: $y/H = 0.14$; dotted line: $y/H = 0.92$. b) Instantaneous vertical profile of C.

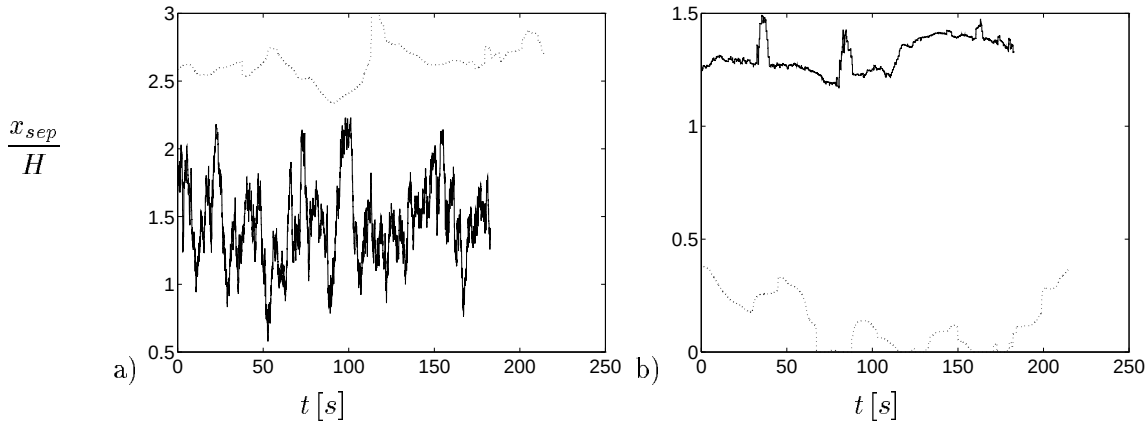

Figure 22. Solid line: spanwise averaged point of separation $\langle x_{sep}/H \rangle_z$; dotted line: point at the centerline $z/H = 0.5$ where $\bar{u}(n = h/2)$ changes sign. n denotes distance from ceiling and floor, respectively. $102 \times 52 \times 52$ mesh. a) Ceiling. b) Floor.

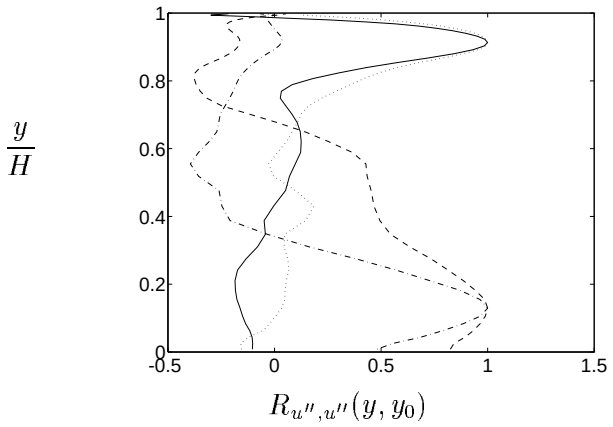

Figure 23. Two-point correlations $R_{u'',u''}(y, y_0)$. $72 \times 52 \times 26$ mesh. Dynamic model. Symmetry plane $z_0/W = 0.5$. Solid line: $x_0/H = 1.0, y_0/H = 0.92$; dotted line: $x_0/H = 2.0, y_0/H = 0.92$; dashed line: $x_0/H = 1.0, y_0/H = 0.14$; dash-dotted line: $x_0/H = 2.0, y_0/H = 0.14$.

The correlation coefficient for the two points in the wall jet at $x_0/H = 1.0$ and $x_0/H = 2.0$ are rather similar near the wall where the peak near the ceiling at $x_0/H = 2.0$ is slightly wider because the thickness of the wall jet is larger. However, the integral lengths are very different (see Table 3) because the negative tail in the $R_{u'',u''}(y, y_0)$ curve at $x_0/H = 1.0$ is much larger than at $x_0/H = 2.0$. This means that at $x_0/H = 1.0$ high $\bar{u}$ velocities in the wall jet are correlated with high negative $\bar{u}$ velocities close to the floor whereas this is not the case at $x_0/H = 2.0$. We find a similar difference for the two points close to the floor. The negative part of $R_{u'',u''}(y, y_0)$ is so strong at $x_0/H = 2.0$ that it almost annihilates the positive part of $R_{u'',u''}(y, y_0)$, which results in a integral length scale close to zero, see Table 3. The integral length scale at $x_0/H = 2.0$ is considerably larger mainly because there is good correlation between the $\bar{u}$ velocity close to the floor and the $\bar{u}$ velocity in the stagnant region up to $y/H \simeq 0.6$.

The probability density function of $\bar{u}$ is shown for four points in Fig. 24, two points in the wall jet and two points in the boundary layer close to the floor. For the points in the wall jet (Fig. 24a) the probability function show a preferred value of $\bar{u}$ showing that the flow has a well defined mean velocity and that the velocity is fluctuating around this mean value. Close to the floor (Fig. 24b) it is hard to find any preferred value of $\bar{u}$ which shows that the flow is irregular and unstable with no well defined mean velocity and large fluctuations.

In Fig. 25 the power density spectrum for the resolved streamwise fluctuation $(u'')^2$ is shown. In fully turbulent flow it should behave as $\Phi \propto n^{(-5/3)}$ (inertial region) which is included as a dashed line. We can see that there is some tendency to inertial region close to $f = 0.2$. This value agrees well with measurements by Sandberg [38]. The sharp decrease of Φ shows that the subgrid model is doing a good job in extracting energy from the resolved flow. The reason why we do not have any distinct inertial region in the spectra may well be connected to insufficient grid resolution. As mentioned on page 20, in connection with the discussion of Fig. 17b, the streamwise vortices in the wall jet region are not resolved properly.

6. Conclusions and Future Work

A numerical procedure for Large Eddy Simulations has been presented for prediction of recirculating flows. A simple Smagorinsky model and a dynamic model was tested. The following conclusions can

x_0/H	y_0/H	z_o/H	Λ_x/H	Λ_y/H	Λ_z/H
1.0	0.92	0.5	-	0.05	-
1.0	0.14	0.5	-	0.24	-
2.0	0.92	0.5	-	0.26	-
2.0	0.14	0.5	-	0.003	-
1.0	$1-h/(2H)$	0.5	0.29	-	-
2.0	$h/(2H)$	0.5	0.43	-	-
1.0	$1-h/(2H)$	0.5	-	-	0.014
2.0	$h/(2H)$	0.5	-	-	0.18

Table 3
Integral length scales.

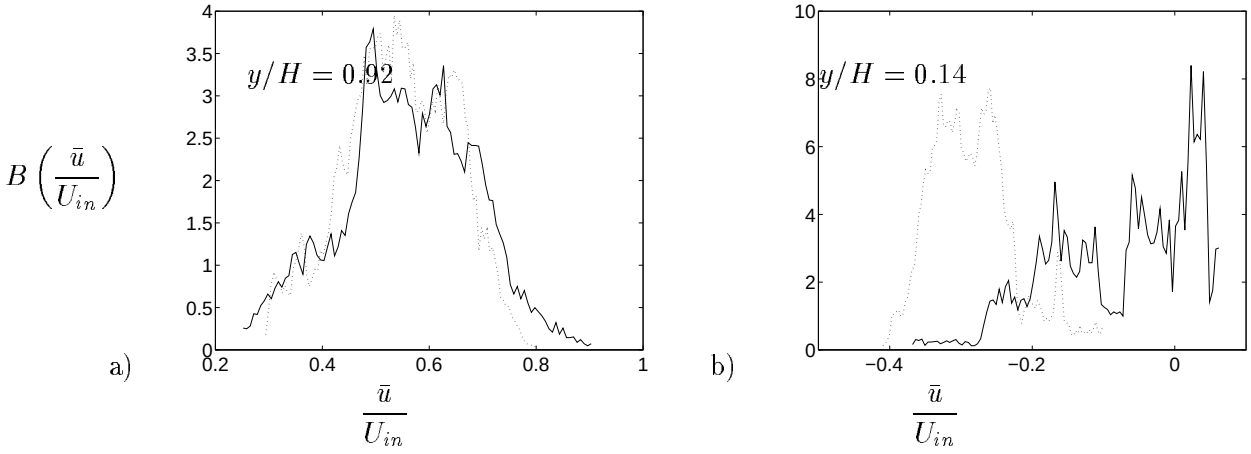

Figure 24. Probability density function of $\bar{u}$. $72 \times 52 \times 26$ mesh. The dynamic model. a) Solid line: $x/H = 1.0$; dotted line: $x/H = 2.0$. b) Solid line: $x/H = 1.0$; dotted line: $x/H = 2.0$;

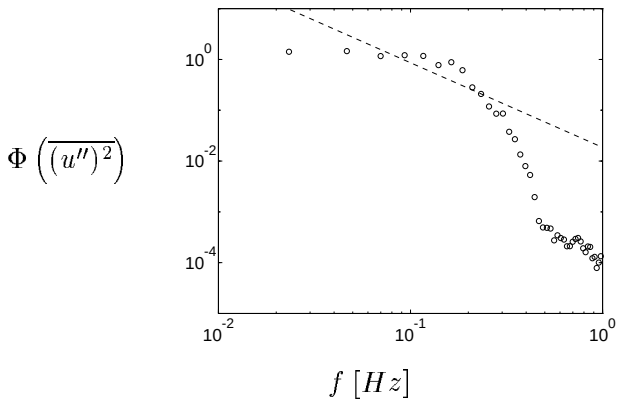

Figure 25. Power density spectrum $\Phi\left(\overline{(u'')^2}\right)$. $72 \times 52 \times 26$ mesh. Dynamic model. Symmetry plane $z/H = 0.5$. $x/H = 2.0, y/H = 0.92$.

be drawn:

- The simple Smagorinsky model was found to be inadequate, because the results were very dependent on the Smagorinsky-constant
- The pressure equation requires some 80 % of the total CPU-time
- The results obtained with the dynamic subgrid model gives results in good agreement with experiments

6.1. Future Work

In an ongoing work [39] we have found the multigrid solver solves the pressure equations more than 10 times faster on fine meshes (1 million nodes). We are also working on solving the whole equation system *implicitly* [39] using the same multigrid solver for the pressure. In the explicit method used in the present work the CFD-number must for stability reasons be below 0.4. With an implicit method the CFL-number is restricted only by concern of accuracy. Using CFL-number of one the implicit method is somewhat faster than the explicit method. If the CFL-number is allowed locally to exceed one (say 2), the implicit method gives a further speed-up of more than two.

REFERENCES

1. LAUNDER B.E. and SPALDING D.B. The numerical computation of turbulent flows. *Computer Methods in Applied Mech. and Eng.*, 3:269–289, 1974.
2. GIBSON M.M. and LAUNDER B.E. Ground effects on pressure fluctuations in the atmospheric boundary layer. *J. Fluid Mech.*, 86:491–511, 1978.
3. DAVIDSON L. Prediction of the flow around an airfoil using a Reynolds stress transport model. *ASME J. Fluid Engng.*, 117:50–57, 1995.
4. DAVIDSON L. Reynolds stress transport modelling of shock-induced separated flow. *Computers & Fluids*, 24:253–268, 1995.
5. LAUNDER B.E. Second-moment closure: Present ... and future? *Int. J. Heat and Fluid Flow*, 10:282–300, 1989.
6. LESCHZINER M.A. Modelling engineering flows with Reynolds stress turbulence closure. *J. Wing Engng. and Ind. Aerodyn.*, 35:21–47, 1991.
7. HANJALIĆ K. Advanced turbulence closure models: A view of current status and future prospects. *Int. J. Heat and Fluid Flow*, 15:178–203, 1994.
8. THOMPSON B.E. Characteristics of a trailing-edge flow with turbulent boundary-layer separation. *Journal of Fluid Mechanics*, 157:305–326, 1985.
9. SMAGORINSKY J. General circulation experiments with the primitive equations. *Monthly Weather Review*, 91:99–165, 1963.
10. GERMANO M.,PIOMELLI U., MOIN P. and CABOT W.H. A dynamic subgrid-scale eddy viscosity model. *Phys. Fluids A*, 3:1760–1765, 1991.
11. E.R. van DRIEST. On turbulent flow near a wall. *J. Aero. Sci.*, 23:1007–1011, 1956.
12. MOIN P. and KIM J. Numerical investigation of turbulent channel flow. *J. Fluid Mech.*, 118:341–377, 1982.
13. JONES W.P. and WILLE M. Large Eddy Simulation of a jet in a cross-flow. In *10th Symp. on Turbulent Shear Flows*, pages 4:1 – 4:6, The Pennsylvania State University, 1995.
14. GERMANO M., PIOMELLI U., MOIN P. and CABOT W.H. Erratum. *Phys. Fluids A*, 3:3128, 1991.
15. LILLY D.K. A proposed modification of the Germano subgrid-scale closure method. *Phys. Fluids A*, 4:633–635, 1992.

16. ZANG Y., STREET R.L. and KOSEFF J.R. A dynamic mixed subgrid-scale model and its application to turbulent recirculating flows. *Phys. Fluids A*, 5:3186–3196, 1993.
17. DAVIDSON L. and FARHANIEH B. CALC-BFC: A finite-volume code employing collocated variable arrangement and cartesian velocity components for computation of fluid flow and heat transfer in complex three-dimensional geometries. Rept. 92/4, Thermo and Fluid Dynamics, Chalmers University of Technology, Gothenburg, 1992.
18. PATANKAR S.V. *Numerical Heat Transfer and Fluid Flow.* McGraw-Hill, New York, 1980.
19. KIM J. and MOIN P. Application of a fractional-step method to incompressible Navier-Stokes equations. *J. Comp. Phys.*, 59:308–323, 1985.
20. ARCHAMBEAU F. *Large Eddy Simulation of Turbulent Vortex Shedding.* PhD thesis, UMIST, Dept. of Mech. Eng., Manchester, UK, 1995.
21. RHIE C.M. and CHOW W.L. Numerical study of the turbulent flow past an airfoil with trailing edge separation. *AIAA J.*, 21:1525–1532, 1983.
22. RENARD J. and GRESSER D. Computational modelling of 2d hill flows. Diploma thesis. rept. 95/6, Thermo and Fluid Dynamics, Chalmers University of Technology, Gothenburg, 1995.
23. BLOSCH E., SHYY W. and SMITH R. The role of mass conservation in pressure-based algorithms. *Numer. Heat Transfer. Part B*, 24:415–429, 1993.
24. LE H. and MOIN P. Direct numerical simulation of turbulent flow over a backward facing step. Report no. tf-58, Stanford University, Dept. Mech. Eng., 1994.
25. RODI W. *Turbulence models and their application in hydraulics - a state of the art review.* International association of Hydraulic Research, Monograph, Delft, 1984.
26. WOLFSHTEIN M. The velocity and temperature distribution in one-dimensional flow with turbulence augmentation and pressure gradient. *Int. J. Mass Heat Transfer*, 12:301–318, 1969.
27. CHEN H.C. and PATEL V.C. Near-wall turbulence models for complex flows including separation. *AIAA J.*, 26:641–648, 1988.
28. LEONARD B.P. A stable and accurate convective modelling based on quadratic upstream interpolation. *Computational Methods in Applied Mechanical Engineering*, 19:59–98, 1979.
29. GHIA U., GHIA K.N. and SHIN T. High-Re solutions for incompressible flow using the Navier-Stokes equations and a multigrid method. *Comp. Phys.*, 48:387–411, 1982.
30. RESTIVO A. *Turbulent Flow in Ventilated Rooms.* PhD thesis, University of London, Imperial College of Science and Technology, Mechanical Engineering Department, 1979.
31. NIELSEN P.V. Specification of a two-dimensional test case. Report, Dept. of Building Technology and Structural Engineering,, Aalborg Universitetscenter, Aalborg, 1990.
32. van LEER B. Towards the ultimate conservative difference scheme. Monotonicity and conservation combined in a second order scheme. *Journal of Computational Physics*, 14:361–370, 1974.
33. YANG K-S and FERZIGER J.H. Large-Eddy simulation of turbulent obstacle flow using a dynamic subgrid-scale model. *AIAA J.*, 31:1406–1413, 1993.
34. S.J, REYNOLDS, W.C., SCHRAUB, F.A. KLINE and RUNSTADLER, P.W. The structure of turbulent boundary layers. *J. Fluid Mech.*, 30:741–773, 1967.
35. KIM J., MOIN P. and MOSER R. Turbulence statistics in fully developed channel flow at low Reynolds number. *J. Fluid Mech.*, 177:133–166, 1987.
36. PIOMELLI U. High Reynolds number calculations using the dynamic subgrid-scale stress model. *Phys. Fluids A*, 5:1484–1490, 1993.
37. HINZE J.O. *Turbulence.* McGraw-Hill, New York, second edition, 1975.
38. SANDBERG M. Velocity characteristics in mechanically ventilated ofice rooms. In *ROOMVENT -87*, volume 2a, Stockholm, 1987.
39. EMVIN P. and DAVIDSON L. Development and implementation of a fast large eddy simulations method. Report (in press), Thermo and Fluid Dynamics, Chalmers University of Technology,

Gothenburg, 1996.